Research Article | Vol. 30, No. 21 / 10 Oct 2022 / Optics Express 37846
Optics EXPRESS

Experimental and theoretical investigation of waveguided plasmonic surface lattice resonances

HÅVARD S. UGULEN,[1,*] RANVEIG FLATABØ,[1] MANSOOR A. SULTAN,[2] JEFFREY T. HASTINGS,[2] AND MARTIN M. GREVE[1]

[1]Department of Physics and Technology, University of Bergen, Allegaten 55, 5007 Bergen, Norway
[2]Department of Electrical and Computer Engineering, University of Kentucky, Lexington, KY, 40506, USA
[*]havard.ugulen@uib.no

Abstract: Plasmonic nanostructures are good candidates for refractive index sensing applications through the surface plasmon resonance due to their strong dependence on the surrounding dielectric media. However, typically low quality-factor limits their application in sensing devices. To improve the quality-factor, we have experimentally and theoretically investigated two-dimensional gold nanoparticle gratings situated on top of a waveguide. The coupling between the localized surface plasmon and waveguide modes results in Fano-type resonances, with high quality-factors, very similar to plasmonic surface lattice resonances. By combining plasmonic surface lattice resonance and waveguide theory, we present a theoretical framework describing the structures. By immersing the fabricated samples in three different media we find a sensitivity of ~50 nm/RIU and figure of merit of 8.9, and demonstrate good agreement with the theory presented. Further analysis show that the sensitivity is very dependent on the waveguide parameters, grating constant and the dielectric environment, and by tuning these parameters we obtain a theoretical sensitivity of 887 nm/RIU.

1. Introduction

The localized surface plasmon resonance is a collective oscillation of the conduction electrons within a conductive nanoparticle of size smaller or comparable to the wavelength of the incident radiation. The electric field of the incident radiation displaces the electrons relative to the positive ion core, creating a dipole with a restoring force. The driving and restoring forces acting on the electrons bound to the particle gives rise to a localized oscillating system with a resonance at a certain frequency. At this frequency the particles' light extinction cross section is significantly increased. The resonance frequency is dependent on the nanoparticle metal, the dielectric environment, and the shape and size of the particle, and may thus be tailored to some extent [1–3].

Optical investigation of metal nanoparticles is commonly performed using extinction spectroscopy, i.e. measuring the fraction of light scattered and absorbed by the sample as a function of wavelength. In the case of a single nanoparticle, the LSPR will manifest itself as a single extinction peak centered at the resonance wavelength. However, arranging the particles in a 1D or 2D grating may significantly alter the extinction spectrum compared to the single particle spectrum. Nanoparticles arranged in close proximity to each other may interact through their near fields [4,5], while far-field interaction may be observed when the light diffracted from the particles interfere to form waves propagating in the plane of the nanoparticle grating, often referred to as Rayleigh anomalies [6–10]. In this case, the particles are subjected to the electric

#470017 https://doi.org/10.1364/OE.470017
Journal © 2022 Received 7 Jul 2022; revised 26 Aug 2022; accepted 12 Sep 2022; published 28 Sep 2022

Optics EXPRESS

field from both the incident wave and the field from the diffracted wave. This results in a new resonance, known as a plasmonic surface lattice resonance (PSLR), or the more general term surface lattice resonance (SLR). Due to the narrow bandwidth of the in-plane diffracted wave, the PSLR extinction peak can be both sharper and have a larger amplitude than the LSPR peak, yielding even greater field enhancement in the nanoparticles. A drawback to this structure is refractive index mismatch between substrate and ambient medium. This makes it difficult to excite PSLRs at normal incidence due to interference between the in-plane diffracted waves and waves reflected from the substrate [11]. Solutions to this problem include making the nanoparticles larger [9], so that the contribution from the reflected waves becomes small compared to the in-plane diffracted waves, or by employing an immersion oil as an index matching layer [8,10].

Another interesting device geometry consists of a nanoparticle grating fabricated on top of a waveguide [12–14]. In these structures, diffracted light from the particles may couple to the waveguide, resulting in propagating waveguide modes. These modes may in turn couple to the LSRP, resulting in a new resonance with extinction features very similar to the PSLR. This can indeed be interpreted as a PSLR, where the LSRP couples with light in the waveguide, rather than light diffracted tangential to the nanoparticle grating (Rayleigh anomalies). Hence, this resonance phenomenon is referred to as waveguided PSLR (WPSLR) for the remainder of this paper. This device geometry has several advantages over the typical PSLR structures. Firstly, the resonance can easily be excited at normal incidence in the WPLSR structure, as opposed to the typical PSLR structures. This is because the coupled diffracted waves propagate in the waveguide rather than in the grating plane. Secondly, the waveguide modes are dependent on both the thickness and refractive index of the waveguide, in addition to the grating constant. Thus, the waveguide offers an additional degree of freedom when tuning the WPSLR wavelength.

The waveguide modes in a dielectric waveguide are sensitive to the refractive index of the sub- and superstrate, i.e. the layers below and above the waveguide material. Due to this sensitivity, combined with the sharpness of the WPSLR extinction peaks, this device has been proposed as a refractive index sensor [15,16]. The figure of merit (FOM) is a common quantity used to compare the performance of different devices, systems, or methods. In the context of the refractive index sensor outlined in this study, the FOM is defined as the refractive index sensitivity divided by the full width at half maximum (FWHM) of the resonance peak, where the sensitivity is calculated as the change in peak wavelength per change in refractive index unit. In a study by Chen et al. a sensitivity for the WPSLR peaks of 250 nm/RIU and a FOM of 28 was demonstrated by numerical calculations, while a sensitivity of 200 nm/RIU was found for the LSPR [15]. Although the sensitivities are similar, the FOM was 14 times larger for the WPSLR peaks due to the much smaller FWHM (narrower peak). There are several other devices reported in the literature that show potential for refractive index sensing [17–19]. A common theme is using coupled resonators to narrow the FWHM, obtaining larger FOM.

In this study, we have performed experimental extinction measurements on structures consisting of a 2D grating of gold nanodisks situated on a waveguide substrate. The experimental results are compared to theoretical spectra calculated from WPSLR theory. To our knowledge, this is the first time this structure is theoretically analyzed in the PSLR framework. Furthermore, extinction spectra are obtained with the samples submerged in three different media, and a refractive index sensitivity is calculated.

2. Theory

The theory section is divided in to three parts. The first part is dedicated to PSLR theory, followed by a description of the gold nanodisk polarizability, and finally, waveguide coupling theory. The combined PSLR and waveguide coupling theory is referred to as WPSLR theory.

Optics EXPRESS

2.1. Surface lattice resonance

The PSLR can be adequately described using the coupled dipole approximation [6,20]. Each particle is treated as an electric dipole which are only susceptible to dipole interactions with the applied electromagnetic field, and the radiated field from the other particles in the array. The polarization induced in a single particle can be expressed as

$$\boldsymbol{P}_i = \alpha \boldsymbol{E}_{\mathrm{loc},i}, \tag{1}$$

where α is the polarizability of the particle and $\boldsymbol{E}_{\mathrm{loc},i}$ is the local electric field at the position of particle i. The local electric field $\boldsymbol{E}_{\mathrm{loc},i}$ can be written as the sum of the incident electric field $\boldsymbol{E}_0$ and the field radiated from all other dipoles in the array,

$$\boldsymbol{E}_{\mathrm{loc},i} = \boldsymbol{E}_0 + \sum_{j \neq i} \boldsymbol{E}_{\mathrm{dipole},j}. \tag{2}$$

Here, $\boldsymbol{E}_{\mathrm{dipole},j}$ is the radiated electric field from dipole j, which in turn can be calculated as

$$\boldsymbol{E}_{\mathrm{dipole,\,j}} = \frac{exp(ikr)}{4\pi\epsilon}\left[k^2 \frac{\hat{\boldsymbol{r}} \times (\hat{\boldsymbol{r}} \times \boldsymbol{P})}{r} + (1 - ikr)\frac{[3(\hat{\boldsymbol{r}} \cdot \boldsymbol{P})\hat{\boldsymbol{r}} - \boldsymbol{P}]}{r^3}\right], \tag{3}$$

where k is the wavenumber, ϵ is the permittivity of the surrounding medium, $\hat{\boldsymbol{r}}$ is the unit vector in the direction of interest, and r is the distance to the point of interest. For a very large array of particles, we can assume that the induced polarization is the same in every particle. Thus, the sum of the field from all dipoles can be written as

$$\sum_{j \neq i} \boldsymbol{E}_{\mathrm{dipole},j} = S\boldsymbol{P}, \tag{4}$$

where the dipole sum S can be expressed as

$$S = \sum_{j \neq i} exp(ikr_{ij})\left[\frac{k^2 \sin^2\theta_{ij}}{r_{ij}} + \frac{(1 - ikr_{ij})(3\cos^2\theta_{ij} - 1)}{r_{ij}^3}\right]. \tag{5}$$

Here, θ_{ij} is the angle between the induced particle polarization vector $\boldsymbol{P}$ and the direction $\hat{\boldsymbol{r}}_{ij}$ from particle i to particle j, and r_{ij} is the distance between the particles. Inserting Eq. (4) and (2) into Eq. (1), one arrives at the following expression for the polarization induced in a single particle

$$\boldsymbol{P} = \frac{\boldsymbol{E}_0}{1/\alpha - S} = \alpha^* \boldsymbol{E}_0, \tag{6}$$

Here, we have defined α^* as the effective polarizability to a single particle in the array subjected to an external driving field $\boldsymbol{E}_0$. The absorption and scattering cross sections can then be calculated as [21]

$$C_{\mathrm{abs}} = 4\pi k\ \mathrm{Im}(\alpha^*) \tag{7}$$

$$C_{\mathrm{sca}} = \frac{8}{3}\pi k^4\ |\alpha^*|^2, \tag{8}$$

and the extinction cross section

$$C_{\mathrm{ext}} = C_{\mathrm{abs}} + C_{\mathrm{sca}}, \tag{9}$$

which is an important quantity as it can be directly compared to experimental extinction spectroscopy measurements.

Optics EXPRESS

2.2. Nanodisk polarizability

The polarizability of the gold nanodisks describe the electric dipole moment induced in the particles when subjected to an external electric field. The gold nanodisks are approximated as spheroids, for which the polarizability α can be expressed as [21]

$$\alpha = abc\frac{\epsilon(\omega) - \epsilon_{\mathrm{m}}}{3\epsilon_{\mathrm{m}} + 3L(\epsilon(\omega) - \epsilon_{\mathrm{m}})}, \tag{10}$$

where $\epsilon(\omega)$ is the dielectric function of the gold particles, ϵ_{m} is the permittivity of the surrounding medium, a, b and c are the semiaxes of the particle, and L is a particle shape factor. To account for the substrate, the refractive index of the surrounding medium is calculated as an effective refractive index [22]

$$n_{\mathrm{eff}} = \frac{1}{2}\left[n_1 + n_2\frac{d}{\lambda} + n_3\left(1 - \frac{d}{\lambda}\right)\right], \tag{11}$$

where n_1, n_2 and n_3 is the refractive index of surrounding medium, waveguide, and substrate, respectively, and d is the thickness of the waveguide. Thus, the permittivity of the surrounding medium ϵ_{m} is replaced by the effective permittivity $\epsilon_{\mathrm{eff}} = n_{\mathrm{eff}}^2$.

The dielectric function of gold can be expressed as [23]

$$\epsilon(\omega) = \epsilon_\infty - \frac{\omega_{\mathrm{p}}^2}{\omega^2 + i\omega\Gamma} + i\Delta\epsilon^{(\mathrm{Au})}(\omega), \tag{12}$$

where ω_{p} is the plasma frequency, Γ is the damping, and ϵ_∞ is the background permittivity accounting for the polarization caused by bound electrons in the metal [24,25]. The term $i\Delta\epsilon^{(\mathrm{Au})}(\omega)$ describes the frequency dependent intraband transitions above $E = 1.8\,\mathrm{eV}$ ($\lambda = 689\,\mathrm{nm}$) and is expressed as

$$i\Delta\epsilon^{(\mathrm{Au})}(\omega) = \frac{iA}{1 + exp(-(\omega - \omega_{\mathrm{c}})/\Delta)}, \tag{13}$$

where the values $A = 5.6$, $\omega_{\mathrm{c}} = 2.4\,\mathrm{eV}$ and $\Delta = 0.17\,\mathrm{eV}$ are derived from experimental data [23]. The damping Γ in Eq. (12) can be written as the sum of three processes so that $\Gamma = \gamma_0 + \gamma_{\mathrm{s}} + \Gamma_{\mathrm{rad}}$. Here, $\gamma_0 = 0.072\,\mathrm{eV}$ represents damping for bulk gold and can be determined from the mean free path of the electrons in the metal. When the particle becomes smaller or comparable to the electron mean free path, the collision frequency increases resulting in additional damping. This effect is accounted for by the term γ_{s} calculated as [26,27]

$$\gamma_{\mathrm{s}} = \frac{Cv_F}{R}, \tag{14}$$

where C is proportionality constant, $v_F = 1.4 \cdot 10^6 m/s$ is the Fermi velocity, and R is the particle radius. The final contribution to the total damping is radiation damping which can be expressed as

$$\Gamma_{\mathrm{rad}} = \frac{h\kappa V}{\pi}, \tag{15}$$

where h is Planck's constant, V is particle volume, and κ is the radiation damping parameter. The values $\omega_{\mathrm{p}} = 9.01\,\mathrm{eV}$, $\epsilon_\infty = 9.84\,\mathrm{eV}$, $C = 0.3$ and $\kappa = 5.5 \cdot 10^{-7} fs^{-1} nm^{-3}$ are taken from the literature [23,26].

Optics EXPRESS

2.3. Waveguide coupling

For light to efficiently propagate in a waveguide, it must interfere constructively with itself within the waveguide. This condition is met when [28]

$$\frac{4\pi d}{\lambda}\sqrt{n_{\mathrm{wg}}^2-\left(\frac{\lambda}{\lambda_{\mathrm{wg}}}\right)^2}=\varphi_{r1}+\varphi_{r2}+2\pi m, \tag{16}$$

where d is the waveguide thickness, n_{wg} is the refractive index of the waveguide, λ is the wavelength in free space, and φ_{r1} and φ_{r2} is the phase shift introduced when the wave is reflected from the upper and lower boundary of the waveguide, respectively. The variable λ_{wg} is related to the propagation constant $\beta=\frac{2\pi}{\lambda_{wg}}$, and is the wavelength of the electromagnetic wave guided by the waveguide. For a dielectric waveguide, the phase shifts φ_1 and φ_2 is dependent on the polarization of the light which can be decomposed into the two polarization states transverse electric (TE) and transverse magnetic (TM). Here, TE and TM refer to the polarization of the light relative to the axis of propagation in the waveguide. Thus, TE polarization means that the electric field oscillates perpendicular to the axis of propagation, and TM means that the magnetic field oscillates perpendicular to the axis of propagation. The phase shift introduced when reflected at the boundary is given by the following equations for TE and TM polarization, respectively

$$\tan\frac{\varphi_r}{2}=\sqrt{\frac{\left(\frac{\lambda}{\lambda_{\mathrm{wg}}}\right)^2-n_{\mathrm{a}}^2}{n_{\mathrm{wg}}^2-\left(\frac{\lambda}{\lambda_{\mathrm{wg}}}\right)^2}} \tag{17a}$$

$$\tan\frac{\varphi_r}{2}=\frac{n_{\mathrm{wg}}^2}{n_{\mathrm{a}}^2}\sqrt{\frac{\left(\frac{\lambda}{\lambda_{\mathrm{wg}}}\right)^2-n_{\mathrm{a}}^2}{n_{\mathrm{wg}}^2-\left(\frac{\lambda}{\lambda_{\mathrm{wg}}}\right)^2}}. \tag{17b}$$

Here, n_{a} is the refractive index of the ambient medium, i.e. the medium surrounding the waveguide. By inserting Eq. (17a) and (17b) into Eq. (16), one arrives at the following dispersion relation for TE and TM polarization, respectively.

$$\lambda=\frac{2\pi d\sqrt{n_{\mathrm{wg}}^2-\left(\frac{\lambda}{\lambda_{\mathrm{wg}}}\right)^2}}{\arctan\left(\sqrt{\frac{\left(\frac{\lambda}{\lambda_{\mathrm{wg}}}\right)^2-n_1^2}{n_{\mathrm{wg}}^2-\left(\frac{\lambda}{\lambda_{\mathrm{wg}}}\right)^2}}\right)+\arctan\left(\sqrt{\frac{\left(\frac{\lambda}{\lambda_{\mathrm{wg}}}\right)^2-n_2^2}{n_{\mathrm{wg}}^2-\left(\frac{\lambda}{\lambda_{\mathrm{wg}}}\right)^2}}\right)} \tag{18a}$$

$$\lambda=\frac{2\pi d\sqrt{n_{\mathrm{wg}}^2-\left(\frac{\lambda}{\lambda_{\mathrm{wg}}}\right)^2}}{\arctan\left(\frac{n_{\mathrm{wg}}^2}{n_1^2}\sqrt{\frac{\left(\frac{\lambda}{\lambda_{\mathrm{wg}}}\right)^2-n_1^2}{n_{\mathrm{wg}}^2-\left(\frac{\lambda}{\lambda_{\mathrm{wg}}}\right)^2}}\right)+\arctan\left(\frac{n_{\mathrm{wg}}^2}{n_2^2}\sqrt{\frac{\left(\frac{\lambda}{\lambda_{\mathrm{wg}}}\right)^2-n_2^2}{n_{\mathrm{wg}}^2-\left(\frac{\lambda}{\lambda_{\mathrm{wg}}}\right)^2}}\right)} \tag{18b}$$

where n_{wg} is the refractive index of the waveguide, and n_1 and n_2 is the refractive index of the lower and upper ambient medium, i.e. the substrate and superstrate. The dispersion relation for TE and TM waveguide modes are presented in Fig. 1. Here, the dispersion is plotted for a waveguide with constant refractive index $n_{\mathrm{wg}}=1.9$ and thickness of $d=150$ nm, and with sub- and superstrate refractive indices $n_1=1.5$ and $n_2=1$, respectively. In addition, the waveguide and substrate light lines are plotted, where only waveguide modes between the two light lines can couple to, and be guided by the waveguide. A light line is calculated from the relation between the free-space wavelength and the wavelength in a given medium. Thus, for the substrate material, the light line is calculated as $\lambda=n_1\lambda_{\mathrm{sub}}$.

Optics EXPRESS

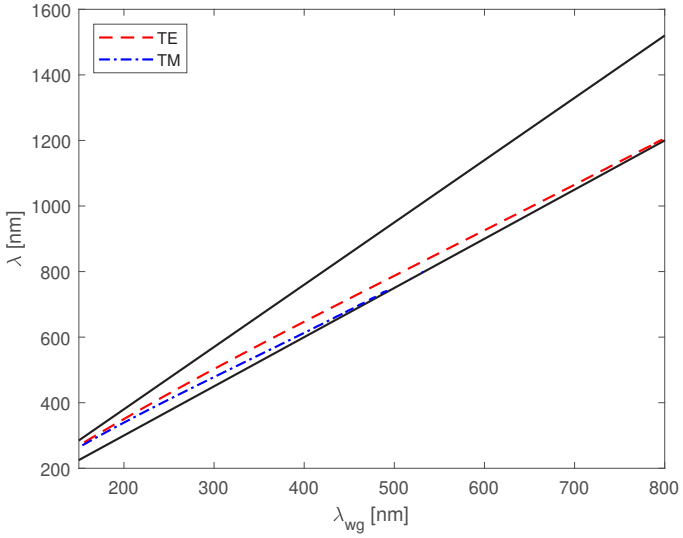

Fig. 1. Dispersion relation for TE (red, dashed) and TM (blue, dash-dotted) waveguide modes calculated for a waveguide thickness $d = 150$ nm and with refractive index $n_{wg} = 1.9$. The substrate and superstrate have refractive indices $n_1 = 1.5$ and $n_2 = 1$, respectively. The black solid lines are the calculated light lines for the waveguide (top) and substrate (bottom).

The position of the waveguide modes relative to the light lines indicate how confined they are to the waveguide [12]. For shorter wavelengths, the waveguide modes are closer to the top light line (given by the waveguide refractive index), hence closely confined to the waveguide and more defined by the waveguide refractive index. For increasing wavelength, the waveguide modes approach the bottom light line, meaning that they penetrate deeper into the sub- and superstrate and become more defined by their refractive indicies. Eventually, the modes intersect the bottom light line (cutoff wavelength), and is no longer bound to the waveguide.

Coupling to the waveguide can be provided by a diffraction grating, where the angle of constructive interference is given by the grating equation

$$a(\sin\theta_i - \sin\theta_m) = m\lambda. \tag{19}$$

Here, a is the grating constant, θ_i is the angle of incidence, θ_m is the angle of diffraction, and $m = 0, \pm1, \pm2, \pm3\cdots$, is the diffraction order. The propagation constant $\beta = \frac{2\pi}{\lambda_{wg}}$ for a wave coupled by the grating is given as [24]

$$\beta = k\sin\theta_i + mg, \tag{20}$$

where $k = \frac{2\pi}{\lambda}$ is the wavenumber of the incident wave, and $g = \frac{2\pi}{a}$ is the reciprocal vector of the grating. For light incident perpendicular to the grating ($\sin\theta_i = 0$), we have

$$\beta = \frac{2\pi}{\lambda_{wg}} = m\frac{2\pi}{a} \Rightarrow \lambda_{wg} = \frac{a}{m}. \tag{21}$$

Inserting Eq. (21) into Eq. (18a) and (18b), one can see that only a discrete set of wavelengths can couple to the waveguide for a given grating constant, resulting in a wavelength selective waveguide.The grating also imposes certain directional limitations. Light is coupled to the waveguide by diffraction such that the directions of the waveguide modes is given by the diffraction pattern of the grating. The most prominent modes will be the first order modes propagating along

Optics EXPRESS

the x- and y-axis. Other modes, such as the first order diagonal modes, will appear at shorter wavelengths.

From Eq. (18a) and (18b), one can see that a change Δn in the refractive index of the substrate or superstrate, leads to a shift in the wavelength of the incident light required to excite a waveguide mode with the wavelength λ_{wg}. In this study, the waveguide is sandwiched between a fixed substrate (glass) and the medium surrounding the sample, acting as the superstrate. The surrounding medium can be altered, e.g. from air to water, resulting in a shift in the exciting wavelength λ calculated as

$$\Delta\lambda = \lambda_2 - \lambda_1, \tag{22}$$

where λ_2 and λ_1 can be calculated from the dispersion relation (Eq. (18a) and (18b)) for the two different surrounding media. The refractive index sensitivity of the waveguide is then given as

$$\text{Sensitivity} = \frac{\Delta\lambda}{\Delta n}. \tag{23}$$

3. Methods

Two-dimensional arrays of gold nanoparticles were fabricated on an ITO covered glass substrate using electron beam lithography. An illustration of the sample geometry is given in Fig. 2. The fabrication process follows the procedure outlined in [29]. The ITO functions as a waveguide and has a thickness of approximately $d = 150\,\text{nm}$. The refractive index of the ITO layer was measured by means of ellipsometry (J. A. Woollam M-2000V), and was found to range from $n_{ITO} = 2.13$ at $\lambda = 450\,\text{nm}$ to $n_{ITO} = 1.86$ at $\lambda = 800\,\text{nm}$. The glass substrate has a refractive index of approximately $n = 1.5$. The gold particle radius was measured in a scanning electron microscope (SEM) and was found to be $R = 50 \pm 5\,\text{nm}$ (see Fig. 3(a)). The particle height was measured by means of atomic force microscopy, giving an average height of $h = 26 \pm 2\,\text{nm}$ (see Fig. 3(b)). Six samples were fabricated, with each particle grating covering $1 \times 1\,\text{mm}$ and with grating constants $a_y = 300\,\text{nm}$ and $a_x = 350 - 475\,\text{nm}$.

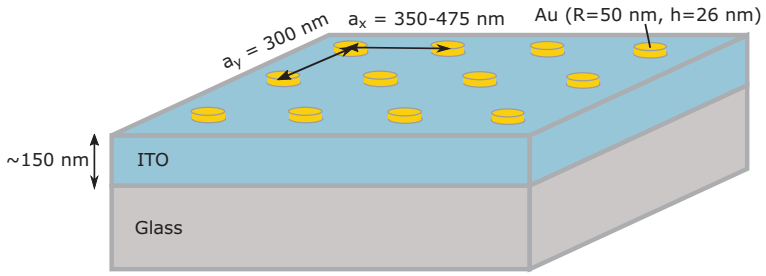

Fig. 2. Illustration of the sample used in the measurement.

The optical investigation of the fabricated samples was performed using transmission spectroscopy to obtain extinction data. A schematic of the setup is given in Fig. 4. White light is directed by means of optical fibre perpendicular to the sample. A beam splitter is placed above the sample, splitting the transmitted light 50/50 to a camera (Thorlabs DCC1545M) to view the sample, and an optical fibre leading to a spectrometer (Ocean Optics USB4000-VIS-NIR-ES) to detect the resulting spectrum. The spectrometer is connected to a computer and the software SpectraSuite is used for data collection. In addition, a rotatabel Glan-Thompson type (ThorLabs GTH5M-A) polarization filter was installed below the sample, so that the incident light polarization could be adjusted. Transmission spectroscopy was performed with the fabricated samples submerged in three different media: air ($n = 1$), water ($n = 1.33$) and a sucrose solution ($n \approx 1.42$). The samples were illuminated with polarized light, corresponding to the excitation of

Optics EXPRESS

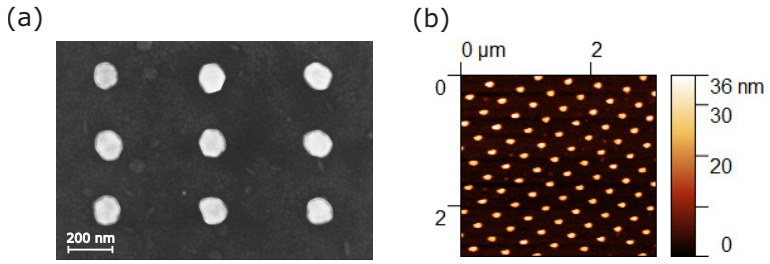

Fig. 3. (a) Close-up SEM image of a few Au nanoparticles from a typical sample. (b) AFM image of a typical sample with particle height indicated by the colorbar.

either TE or TM waveguide modes propagating along the x-axis in the waveguide. Attenuation by the substrate was accounted for by subtracting the extinction spectrum of the samples at a location where there were no particles.

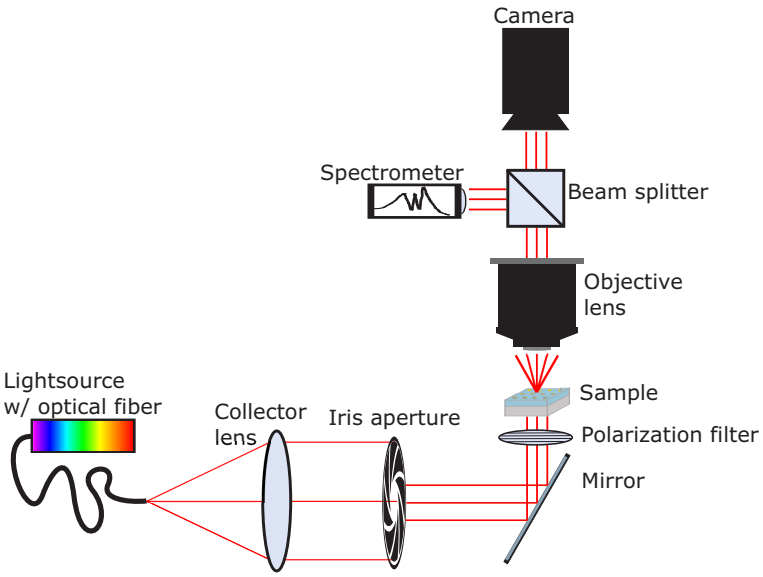

Fig. 4. Schematic of the transmission spectroscopy setup.

4. Results and discussion

4.1. Experimental results

The results from the transmission spectroscopy are presented in Fig. 5. The general shape of the extinction plot displays features similar to a typical PSLR extinction plot. For all samples, the isolated particle LSPR is observed as a single broad peak centered somewhere between 600 – 625 nm. Due to presence of the waveguide modes, additional peaks and dips are observed in the extinction spectra. For larger grating constants, the waveguide modes are excited at longer wavelenghts than the LSPR peak, and manifest themselves as sharp extinction peaks. As the grating constant decreases the waveguide modes are excited at shorter wavelenghts, and eventually within the LSPR peak, where they now manifest themselves as dips in the LSPR peak.

From Fig. 5, one can see that the WPSLR peaks and dips come in pairs. This is due to the periodically arranged nanoparticles on top of the waveguide, resulting in a stop band at the center

Optics EXPRESS

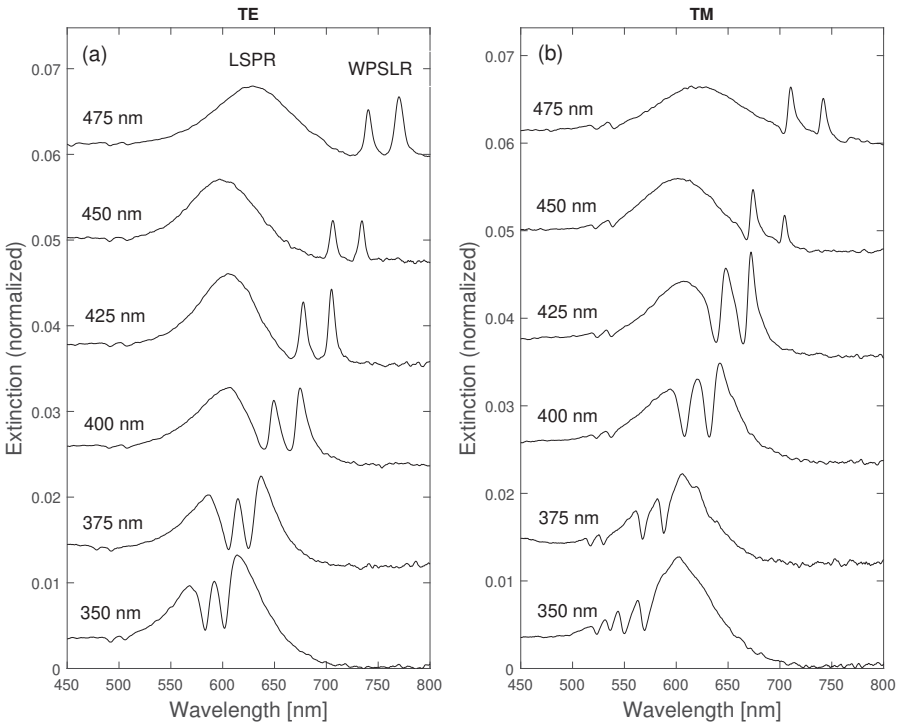

Fig. 5. Experimental extinction spectra for grating constant a_x along the x-axis varying from 350 nm-475 nm (bottom to top) in 25 nm steps, and with grating constant $a_y = 300$ nm along the y-axis. To avoid overlapping plots, the zero line is shifted up for each plot. The plots are normalized so that the integral over each plot with respect to its zero line is equal to 1. (a) TE polarization. (b) TM polarization.

and the edges of the first Brillouin zone [13,30]. Incident light of wavelengths within this stop band cannot excite waveguide modes. Thus, when the light is incident with a slight angle, or the incident beam is not exactly parallel, the waveguide mode is split into two modes excited by wavelengths on opposite sides of the stop band. Two small dips can also be observed on the left side of the broad LSPR peak. These dips are the result of the waves propagating along the y-axis in the waveguide (see Fig. 2), where the grating constant is 300 nm for all samples. The waves propagating along the x- and y-axis have opposite polarization with respect to their direction of propagation in the waveguide. Thus, for the spectra labeled TE, the polarization of the waveguide mode is TE in the x-direction and TM in the y-direction, and vice versa for the spectra labeled TM. The features associated with the waveguide modes can be observed at longer wavelengths for TE polarization than for TM polarization, which is consistent with the dispersion relation plotted in Fig. 1. The polarization of the modes excited in the waveguide is controlled by the polarization of the incident light, which is linearly polarized along the y-axis in Fig. 5(a), and along the x-axis in Fig. 5(b). Using either unpolarized light, or light polarized along the diagonal of the grating, one would excite both TE and TM modes along both the x- and y-axis, resulting in twice the number of coupled modes and corresponding dips/peaks in the extinction spectra.

In order to analyze the extinction sepctra presented in Fig. 5, we turn to the WPSLR theory presented in Section 2. The wavevector k in Eq. (5) is calculated from the dispersion relation (Eq. (18a) and (18b)), so that $k = k_{\mathrm{wg}} = 2\pi/\lambda_{\mathrm{wg}}$. Waveguide, particle and grating parameters are equal to those given in Section 3. In order to account for the small tilt in the sample, the

Optics EXPRESS

calculated waveguide mode is split into two modes with wavevectors $k_{\pm} = k \pm \Delta k$, where Δk is chosen to give a good fit with the experimental data.

To understand the interaction we do a detailed analysis of two different cases (see Fig. 6 and 7). The first case is when the waveguide modes are excited at longer wavelengths than the LSPR peak. In Fig. 6(a), the experimental plot for TE polarization and a grating constant of 450 nm (same as in Fig. 5(a)) is compared to a theoretical plot calculated from the WPSLR theory. In Fig. 6(b), theoretical values for the absolute value of the inverse of the isolated particle polariziability $|1/\alpha|$ and the absolute value of the dipole sum $|S|$, is plotted together with the the absolute value of the inverse of the effective polarizability of a gold nanoparticle in a 2D grid, given as $|1/\alpha^*| = |1/\alpha - S|$. The WPSLR calculation is performed for a grating consisting of 2000 particles.

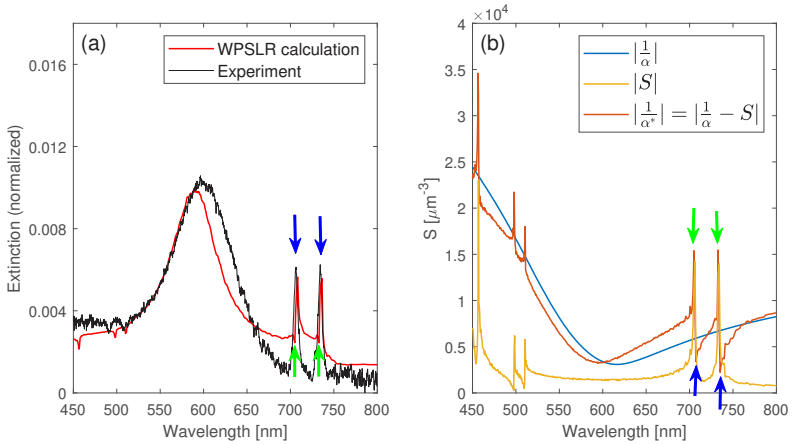

Fig. 6. (a) Experimental (black) and calculated (red) extinction spectrum for a grating constant of $a = 450$ nm and TE polarization. The plots are normalized so that the integral over each plot is equal to 1. (b) A plot of the absolute value of the inverse of the single particle polarizability, $|\frac{1}{\alpha}|$ (blue), the dipole sum, $|S|$ (yellow), and the inverse of the effective polarizability, $|\frac{1}{\alpha^*}| = |\frac{1}{\alpha} - S|$ (red). The color of the arrows indicate the corresponding features across Fig. (a) and Fig. (b).

Overall, there is qualitatively good agreement between the experimental and theoretical extinction spectrum in Fig. 6(a). According to Eq. (8), the scattering cross section is resonantly enhanced when $|\alpha^*|$ becomes large, i.e. when $|1/\alpha^*|$ becomes small. This is clearly demonstrated where the peaks (local maxima) in the WPSLR extinction plot in Fig. 6(a) coincides with the local minima in the plot of $|\frac{1}{\alpha^*}|$ in Fig. 6(b). Conversely, dips in the extinction spectrum coincide with local maxima in $|\frac{1}{\alpha^*}|$. In Fig. 6(b), one can see that the dipole sum S, i.e. the scattered field coupled to the waveguide, interacts with the inverse of the isolated particle polarizability $\frac{1}{\alpha}$ in either a constructive or destructive way. There are two peaks in the dipole sum located around 720 nm in Fig. 6(b). These peaks correspond to the waveguide modes propagating along the x-axis, where the IPD is 450 nm. Here, the interaction between S and $\frac{1}{\alpha}$ abruptly changes from constructive to destructive, as seen by the rapid change in $|\frac{1}{\alpha^*}|$. The peaks in $|\frac{1}{\alpha^*}|$ results in the small dips barely observable in the PLSR extinction spectrum. This relation between $|\frac{1}{\alpha^*}|$ and extinction is indicated by the green arrows in Fig. 6(a) and (b). The peaks in $|\frac{1}{\alpha^*}|$ are immediately followed by dips, resulting in the WPSLR peaks observed in the extinction spectrum, as indicated by the blue arrows. The abrupt change from constructive to destructive interaction is due to the interference between a narrow resonance (the waveguide modes), with a rapidly changing phase,

Optics EXPRESS

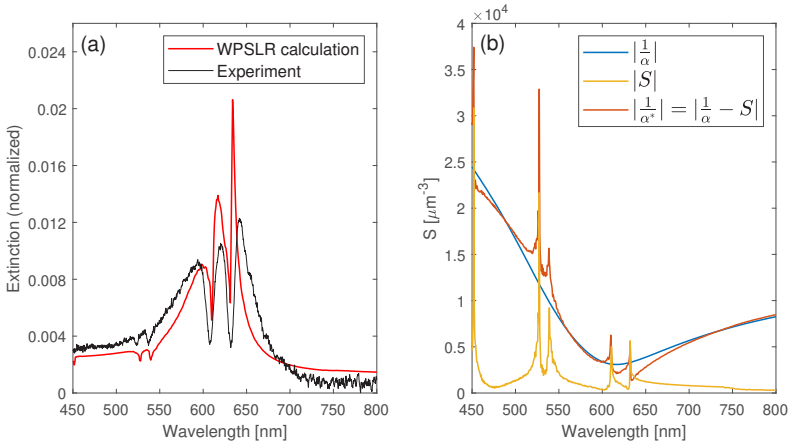

Fig. 7. (a) Experimental (black) and calculated (red) extinction spectrum for a grating constant of $a = 400$ nm and TM polarization. The plots are normalized so that the integral over each plot is equal to 1. (b) A plot of the absolute value of the inverse of the single particle polarizability, $|\frac{1}{\alpha}|$ (blue), the dipole sum, $|S|$ (yellow), and the inverse of the effective polarizability, $|\frac{1}{\alpha^*}| = |\frac{1}{\alpha} - S|$ (red).

and a broad resonance (LSPR), with a slowly changing phase. Such resonances are often referred to as a Fano-type resonances, which are known for their highly asymmetric shape [8,31,32].

There are also two peaks in the dipole sum located around 500 nm in Fig. 6(b). These peaks correspond to the waveguide modes propagating along the y-axis, where the IPD is 300 nm. The corresponding dips in the extinction spectrum are very small due to the fact that the extinction in this part of the spectrum is already very low. It should also be mentioned that there is a pair of peaks in the dipole sum around 450 nm (only one is within the plotted range), which is the result of the waveguide modes propagating along the diagonal of the particle grating. The effect of these peaks are not observed in the experimental extinction spectrum, which could be due to a low signal-to-noise ratio.

The second case, when the waveguide modes are located within the LSPR peak, are analyzed by comparing experimental results to calculations for TM polarization and a grating constant of 400 nm (same as in Fig. 5(b)). The results are presented in Fig. 7.

Again, one can see from Fig. 7(a) that the theory is in qualitatively good agreement with the experimental results. Focusing on the LSPR, there are two peaks in the dipole sum S located around 620 nm. Here, the dipole sum peaks interacts mainly constructively with the inverse of the isolated particle polarizability $\frac{1}{\alpha}$. This results in peaks in the effective polarizability $\frac{1}{\alpha^*}$, and consequently, the dips observed in the LSPR peak in the WPLSR extinction plot. At approximately 640 nm, the right shoulder of the dipole sum peak interacts destructively with the inverse of single particle polarizability, such that $|1/\alpha^*|$ becomes small, resulting in the observed extinction peak.

4.2. Sensitivity analysis

By comparing extinction spectra from transmission measurements performed with the samples submerged in air, water and sucrose, a refractive index sensitivity can be calculated according to Eq. (23). Theoretical extinction spectra are compared to experimental results for TE polarization in Fig. 8(a) and for TM polarization in Fig. 8(b), both with an IPD of 450 nm. Here, the extinction is plotted for both air ($n = 1$), water ($n = 1.33$) and a sucrose solution ($n \approx 1.42$).

Optics EXPRESS

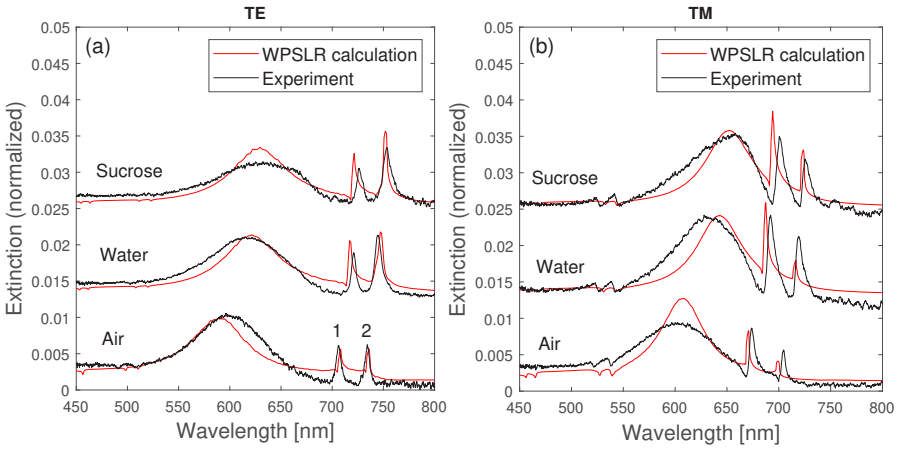

Fig. 8. Experimental (black) and calculated (red) extinction spectra for a grating constant of 450 nm and with the sample submerged in air, water and a sucrose solution. (a) TE polarization. (b) TM polarization.

From Fig. 8 one can see that both the LSPR peak and the WPSLR peaks shift to longer wavelengths with increasing refractive index. For both TE and TM polarization, the shift is accurately predicted by the WPSLR theory, although the TM WPSLR peaks appear at slightly shorter wavelengths compared to the experimental spectra. As the WPSLR peaks position is mainly determined by the waveguide parameters and refractive index of the surrounding media (i.e. Equation (18)), the discrepancies seen between theory and experiment is likely due to uncertainties in these, e.g. waveguide thickness and refractive index. Also, the model does not consider the contribution from the gold particles to the effective refractive index of the superstrate when calculating the waveguide modes. It can also be seen that there is some deviations in the LSPR peak position. This discrepancy is more likely due to the modeling of the single particle polarizability, such as uncertainties in the dielectric function, and the fact that the particles are modeled as spheroids. The model does also not include retardation, which have a very small effect due to the small particle height of 26 nm. The rather simple approximation for the effective dielectric environment approximation, Eq. (11), is also expected to have an influence on the simulated LSPR peak position.

As the theoretical extinction spectra is calculated for discrete wavelengths, one may in some cases calculate the extinction cross section for frequencies closer to the resonance center frequency than in others. For instance, the dipole sum S and the inverse of the single particle polarizability may almost completely cancel each other out at specific wavelengths, resulting in unreasonably large extinction peaks (see Eq. (6)). Hence, a moving average is used for the theoretical extinction spectra, resulting in comparable peak height and width to the experimental spectra. The applied averaging interval affects both the height and the width of the peaks. Using a smaller interval, the peaks become taller and sharper as demonstrated in Fig. 9.

Using an averaging interval of 2.4 nm, the average FWHM is measured to be 2.4 nm, while a FWHM of 1.2 nm is measured for an averaging interval of 0.21 nm. Thus, using the the smaller averaging interval would result in a two times larger FOM. The averaging interval of 0.21 nm used in Fig. 9(b), is comparable to the optical resolution of the spectrometer used for the experimental measurements, and should be the most accurate representation of the theoretical spectrum. As can can be seen, the theoretical spectrum displays much taller and sharper peaks than the experimental spectrum. This is expected as the theoretical calculation is based on a perfect sample, where all particles and inter-particle distances are identical, and the ITO (waveguide) layer is perfectly

Optics EXPRESS

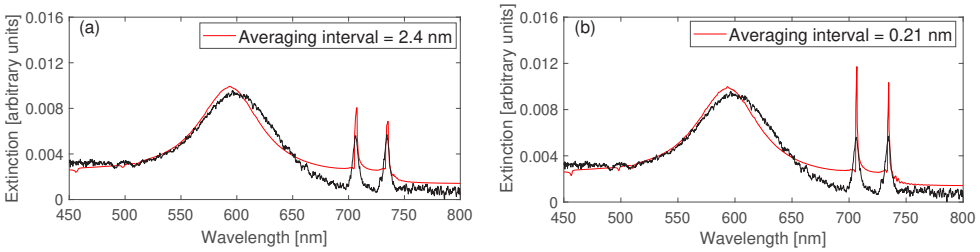

Fig. 9. Experimental (black) and calculated (red) extinction spectra for a grating constant of $a = 450$ nm and TE polarization. The calculated extinction spectra is calculated with an averaging interval of (a) 2.4 nm and (b) 0.21 nm.

homogeneous with the same thickness everywhere. This will not be true for the experimental samples, where variations in particle size and shape, and variation in the ITO layer will cause a broadening of the resonance peaks.

The sensitivity of the WPSLR peaks can be calculated according to Eq. (23), where the peak position is determined by the point of highest intensity. In Table 1 (TE polarization) and 2 (TM polarization), the sensitivities and FOMs measured from the experimental and the calculated spectra in Fig. 8 are compared, in addition to the sensitivity of the waveguide modes calculated from the dispersion relation (Eq. (18a) and (18b). The FOM is calculated using the average FWHM of the peaks for the three different surrounding media.

Table 1. WPSLR peak wavelength, refractive index sensitivity, and FOM for a grating constant of 450 nm and TE polarization. Peak number is indicated in Fig. 8.

		Peak wavelength [nm]			$\frac{\Delta\lambda}{\Delta n}$ [$\frac{\text{nm}}{\text{RIU}}$]	FOM
	Peak nr.	Air	Water	Sucrose		
Experiment	1	706	722	727	50	8.9
	2	734	745	753	45	6.3
WPSLR	1	708	718	721	31	7.2
	2	736	747	752	38	8.6
Waveguide	1	718	728	733	36	

Table 2. WPSLR peak wavelength, refractive index sensitivity, and FOM for a grating constant of 450 nm and TM polarization. Peak number is indicated in Fig. 8.

		Peak wavelength [nm]			$\frac{\Delta\lambda}{\Delta n}$ [$\frac{\text{nm}}{\text{RIU}}$]	FOM
	Peak nr.	Air	Water	Sucrose		
Experiment	1	674	692	701	64	8.5
	2	705	720	725	48	7.1
WPSLR	1	671	687	694	55	15.3
	2	699	717	724	60	17.8
Waveguide	1	682	700	703	50	

For TE polarization, the predicted sensitivity is smaller than the observed experimental sensitivity, while for TM polarization, the theoretical and experimental sensitivities are similar. Both theory and experiment show larger sensitivities for TM polarization than for TE polarization. This is consistent with the dispersion relation plotted in Fig. 1, demonstrating that the TM modes

Optics EXPRESS

are less confined to the waveguide, hence more sensitive to changes in the surrounding medium. The WPSLR and waveguide sensitivities are very similar, which is expected as the dipole sum peaks are determined by the waveguide dispersion relation. For TE polarization (Table 1), similar FOMs are calculated for the experimental and theoretical spectra. However, this is not case for TM polarization (Table 2), where calculated spectra have FOMs approximately two times larger than the FOMs of the experimental spectra. As previously discussed, the FOMs obtained for the calculated spectra is dependent on the averaging interval used. Thus, theoretical and experimental FOMs are not very comparable. Using the FWHM obtained from spectrum in Fig. 9(b) for TE polarization, a FOM of 39 is obtained, which is over four times larger than the FOM obtained from Fig. 8.

Both the experimental sensitivities and FOMs obtained in this work are quite far from the theoretically predicted sensitivity of 250 nm/RIU and FOM of 28 obtained from numerical calculations by Chen et al. [15], although the samples investigated are very similar in terms of waveguide refractive index and thickness. The main difference between the two structures is the grating constant along the axis of propagation. For the sensitivity analysis performed here, a grating constant of 450 nm was used, resulting in WPSLR peaks ranging from 675 – 750 nm (depending on polarization and surrounding medium). The grating constants used in this study were selected mainly due to being optically addressable for the experimental measurements. On the other hand, Chen et al. used a grating constant of 700 nm, resulting in WPSLR peaks around 1100 nm.

In order to investigate how the sensitivity depends on the grating constant a, the sensitivity is calculated from the dispersion relation for TM polarization (Eq. (18b)) and plotted as a function of waveguide wavelength λ_{wg}, where $\lambda_{wg} = a$ for first order modes ($m = 1$ in Eq. (21)). Furthermore, the sensitivity is plotted for different combinations of waveguide refractive index and waveguide thickness, demonstrating the dependency on the waveguide parameters.

From Fig. 10, it can be seen that the maximum obtainable sensitivity increases with both waveguide refractive index and thickness. In general, the sensitivity increases with the grating constant $a = \lambda_{\mathrm{wg}}$ up to a certain point, then decrease until reaching the cutoff wavelength. The sensitivities are calculated for a refractive index of the surrounding medium changing from $n_a = 1$ (air) to $n_a = 1.42$ (sucrose solution). However, the sensitivity is not expected to be constant over

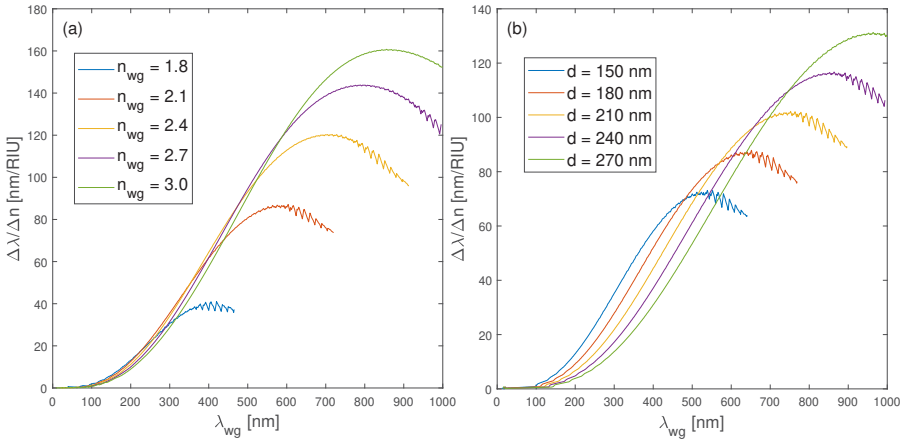

Fig. 10. Theoretical WPSLR sensitivity as a function of waveguide wavelength λ_{wg}. (a) Sensitivity for increasing waveguide refractive index n_{wg} and constant waveguide thickness $d = 150$ nm. (b) Sensitivity for increasing waveguide thickness d and constant waveguide refractive index $n_{\mathrm{wg}} = 2$.

Optics EXPRESS

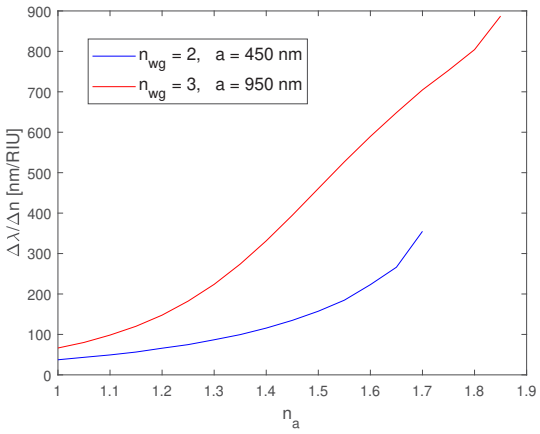

Fig. 11. Theoretical WPSLR sensitivity as a function of surrounding medium refractive index n_a. For a waveguide of thickness $d = 150$ nm, refractive index $n_{\mathrm{wg}} = 2$, and with grating constant $a = \lambda_{\mathrm{wg}} = 450$ nm (blue). For a waveguide of thickness $d = 150$ nm, refractive index $n_{\mathrm{wg}} = 3$, and with grating constant $a = \lambda_{\mathrm{wg}} = 850$ nm (red).

the range $n_a = 1 - 1.42$, but vary with the refractive index of the surrounding medium. In Fig. 11, the sensitivity is plotted as a function of the refractive index of the surrounding medium. The sensitivity is plotted for two different combinations of waveguide refractive index and grating constant.

For both cases presented in Fig. 11, the sensitivity increases significantly with increasing refractive index of the surrounding medium. A maximum sensitivity is reach when the waveguide mode lies at the bottom light line (see Fig. 1), i.e. at the cutoff wavelength. At this point, the waveguide modes reach a maximum penetration depth into the surrounding medium, while still being bound to the waveguide. This is also the theoretical maximum refractive index at which the device can measure changes in the surrounding medium. For the combination of waveguide refractive index $n_{\mathrm{wg}} = 2$ and a grating constant of $a = 450$ nm (similar to the experimental structure investigated in Fig. 8), the maximum sensitivity (and refractive index limit) is reach at $n_a = 1.7$, resulting in a sensitivity of 355 nm/RIU. A much higher sensitivity can be obtained by increasing the waveguide refractive index to $n_{\mathrm{wg}} = 3$ and grating constant to $a = 950$ nm, reaching 887 nm/RIU at $n_a = 1.85$.

5. Summary and conclusion

Structures consisting of a 2D gold nanoparticle grating situated on top of a dielectric waveguide have been fabricated by means of electron beam lithography. Experimental investigation of the fabricated samples are preformed using transmission spectroscopy, and extinction spectra are obtained for both TE and TM polarization. Combining PSLR and waveguide theory, a theoretical framework has been developed, yielding qualitatively good agreement between experimental and theoretically calculated extinction spectra. This approach provide valuable insight into the physics behind the observed extinction spectra.

The refractive index sensitivity of the samples has been investigated, obtaining both experimental and theoretically calculated spectra for the samples submerged in air, water and a sucrose solution. Analysing the sample with a grating constant of 450 nm, the sensitivity and FOM for the WPSLR peaks were calculated for both the theoretical and experimental spectra. From experiment, we obtained a sensitivity of 50 nm/RIU and FOM of 8.9 for TE polarization, while a sensitivity of 64 nm/RIU and FOM of 8.5 was obtained for TM polarization. For the calculated

Optics EXPRESS

spectra, a similar sensitivity of 60 nm/RIU was found for TM polarization, while a slightly lower sensitivity of 38 nm/RIU was found for TE polarization. Comparing experimental and calculated spectra, it is shown that much larger FOMs could be obtained for the calculated spectra, depending on the averaging interval used for the calculated extinction cross section. Using an averaging interval of 0.21 nm, which is similar to the optical resolution of the spectrometer, a FOM of 39 was obtained. However, it is uncertain if this is achievable experimentally, as experimental limitations is expected due to inherent properties in the sample (film and particle uniformity).

Finally, by calculating the waveguide sensitivity directly from the waveguide dispersion relation, we find that the sensitivity can be increased by increasing the waveguide refractive index, thickness, and the grating constant. For a waveguide with thickness $d = 150$ nm, the maximum sensitivity can be increased from 34 nm/RIU to 160 nm/RIU by increasing the waveguide refractive index from $n = 1.8$ to $n = 3.0$, and the grating constant from $a = 420$ nm to $a = 860$ nm. Additionally, the sensitivity is found to increase significantly with the refractive index of the surrounding medium. A sensitivity of 887 nm/RIU is predicted for a waveguide with refractive index $n_{\mathrm{wg}} = 3$, thickness $d = 150$ nm and grating constant $a = 950$, for a surrounding medium with refractive index $n_a = 1.85$.

Funding. Universitetet i Bergen.

Disclosures. The authors declare no conflicts of interest.

Data availability. Data underlying the results presented in this paper are not publicly available at this time but may be obtained from the authors upon reasonable request.

References

1. W. Ni, X. Kou, Z. Yang, and J. Wang, "Tailoring longitudinal surface plasmon wavelengths, scattering and absorption cross sections of gold nanorods," ACS Nano **2**(4), 677–686 (2008).
2. H. Huang, S. Huang, S. Yuan, C. Qu, Y. Chen, Z. Xu, B. Liao, Y. Zeng, and P. K. Chu, "High-sensitivity biosensors fabricated by tailoring the localized surface plasmon resonance property of core–shell gold nanorods," Anal. Chim. Acta **683**(2), 242–247 (2011).
3. P. K. Kuiri, "Tailoring localized surface plasmons in ag–al alloys' nanoparticles," J. Alloys Compd. **826**, 154250 (2020).
4. A. E. Schlather, N. Large, A. S. Urban, P. Nordlander, and N. J. Halas, "Near-field mediated plexcitonic coupling and giant rabi splitting in individual metallic dimers," Nano Lett. **13**(7), 3281–3286 (2013).
5. K.-H. Su, Q.-H. Wei, X. Zhang, J. Mock, D. R. Smith, and S. Schultz, "Interparticle coupling effects on plasmon resonances of nanogold particles," Nano Lett. **3**(8), 1087–1090 (2003).
6. A. D. Humphrey and W. L. Barnes, "Plasmonic surface lattice resonances on arrays of different lattice symmetry," Phys. Rev. B **90**(7), 075404 (2014).
7. A. Humphrey and W. Barnes, "Plasmonic surface lattice resonances in arrays of metallic nanoparticle dimers," J. Opt. **18**(3), 035005 (2016).
8. A. Väkeväinen, R. Moerland, H. Rekola, A.-P. Eskelinen, J.-P. Martikainen, D.-H. Kim, and P. Törmä, "Plasmonic surface lattice resonances at the strong coupling regime," Nano Lett. **14**(4), 1721–1727 (2014).
9. V. Kravets, F. Schedin, and A. Grigorenko, "Extremely narrow plasmon resonances based on diffraction coupling of localized plasmons in arrays of metallic nanoparticles," Phys. Rev. Lett. **101**(8), 087403 (2008).
10. B. Auguié and W. L. Barnes, "Collective resonances in gold nanoparticle arrays," Phys. Rev. Lett. **101**(14), 143902 (2008).
11. B. Auguié, X. M. Bendana, W. L. Barnes, and F. J. G. de Abajo, "Diffractive arrays of gold nanoparticles near an interface: Critical role of the substrate," Phys. Rev. B **82**(15), 155447 (2010).
12. S. Linden, J. Kuhl, and H. Giessen, "Controlling the interaction between light and gold nanoparticles: selective suppression of extinction," Phys. Rev. Lett. **86**(20), 4688–4691 (2001).
13. A. Christ, T. Zentgraf, J. Kuhl, S. Tikhodeev, N. Gippius, and H. Giessen, "Optical properties of planar metallic photonic crystal structures: Experiment and theory," Phys. Rev. B **70**(12), 125113 (2004).
14. V. Yannopapas and N. Stefanou, "Optical excitation of coupled waveguide-particle plasmon modes: A theoretical analysis," Phys. Rev. B **69**(1), 012408 (2004).
15. J. Chen, J. Yuan, Q. Zhang, H. Ge, C. Tang, Y. Liu, and B. Guo, "Dielectric waveguide-enhanced localized surface plasmon resonance refractive index sensing," Opt. Mater. Express **8**(2), 342–347 (2018).
16. P. Huang, Y. Yao, W. Zhong, P. Gu, Z. Yan, F. Liu, B. Yan, C. Tang, J. Chen, and M. Zhu, "Optical sensing based on classical analogy of double electromagnetically induced transparencies," Results Phys. **39**, 105732 (2022).
17. J. Chen, W. Fan, T. Zhang, C. Tang, X. Chen, J. Wu, D. Li, and Y. Yu, "Engineering the magnetic plasmon resonances of metamaterials for high-quality sensing," Opt. Express **25**(4), 3675–3681 (2017).

Optics EXPRESS

18. J. Chen, H. Nie, C. Tang, Y. Cui, B. Yan, Z. Zhang, Y. Kong, Z. Xu, and P. Cai, "Highly sensitive refractive-index sensor based on strong magnetic resonance in metamaterials," Appl. Phys. Express **12**(5), 052015 (2019).
19. J. Chen, Y. Kuang, P. Gu, S. Feng, Y. Zhu, C. Tang, Y. Guo, Z. Liu, and F. Gao, "Strong magnetic plasmon resonance in a simple metasurface for high-quality sensing," J. Lightwave Technol. **39**(13), 4525–4528 (2021).
20. V. G. Kravets, A. V. Kabashin, W. L. Barnes, and A. N. Grigorenko, "Plasmonic surface lattice resonances: a review of properties and applications," Chem. Rev. **118**(12), 5912–5951 (2018).
21. C. F. Bohren and D. R. Huffman, *Absorption and scattering of light by small particles* (John Wiley & Sons, 2008).
22. E. Simsek, "On the surface plasmon resonance modes of metal nanoparticle chains and arrays," Plasmonics **4**(3), 223–230 (2009).
23. A. Derkachova, K. Kolwas, and I. Demchenko, "Dielectric function for gold in plasmonics applications: size dependence of plasmon resonance frequencies and damping rates for nanospheres," Plasmonics **11**(3), 941–951 (2016).
24. S. A. Maier, *Plasmonics: fundamentals and applications*, vol. 1 (Springer, 2007).
25. K. Kolwas and A. Derkachova, "Damping rates of surface plasmons for particles of size from nano-to micrometers; reduction of the nonradiative decay," J. Quant. Spectrosc. Radiat. Transf. **114**, 45–55 (2013).
26. C. Novo, D. Gomez, J. Perez-Juste, Z. Zhang, H. Petrova, M. Reismann, P. Mulvaney, and G. V. Hartland, "Contributions from radiation damping and surface scattering to the linewidth of the longitudinal plasmon band of gold nanorods: a single particle study," Phys. Chem. Chem. Phys. **8**(30), 3540–3546 (2006).
27. V. Juvé, M. F. Cardinal, A. Lombardi, A. Crut, P. Maioli, J. Pérez-Juste, L. M. Liz-Marzán, N. Del Fatti, and F. Vallée, "Size-dependent surface plasmon resonance broadening in nonspherical nanoparticles: single gold nanorods," Nano Lett. **13**(5), 2234–2240 (2013).
28. B. E. Saleh and M. C. Teich, *Fundamentals of photonics* (john Wiley & sons, 2007).
29. M. M. Greve, T. O. Håvardstun, and B. Holst, "Measuring the localized surface plasmon resonance effect on large arrays (5 mm× 5 mm) of gold and aluminum nanoparticles on borosilicate glass substrates, fabricated by electron beam lithography," J. Vac. Sci. & Technol. B, Nanotechnol. Microelectron. Materials, Process. Meas. Phenom. **31**, 06F410 (2013).
30. S. G. Tikhodeev, A. Yablonskii, E. Muljarov, N. A. Gippius, and T. Ishihara, "Quasiguided modes and optical properties of photonic crystal slabs," Phys. Rev. B **66**(4), 045102 (2002).
31. Y. Huang, L. Ma, M. Hou, and Z. Zhang, "Universal near-field interference patterns of fano resonances in two-dimensional plasmonic crystals," Plasmonics **11**(5), 1377–1383 (2016).
32. Y. Francescato, V. Giannini, and S. A. Maier, "Plasmonic systems unveiled by fano resonances," ACS Nano **6**(2), 1830–1838 (2012).